



Cite this: *J. Mater. Chem. C*, 2022, 10, 6043

Isomer engineering of dipyrido[3,2-a:3',4'-c]phenazine-acceptor-based red thermally activated delayed fluorescent emitters†

Shantaram Kothavale, Won Jae Chung and Jun Yeob Lee  *

To determine the effect of donor substitution pattern on emission properties, we designed and synthesized two isomeric red thermally activated delayed fluorescent (TADF) emitters, *i.e.*, 11,12-bis(9,9-dimethylacridin-10(9H)-yl)dipyrido[3,2-a:2',3'-c]phenazine (**oDMAC-DPPZ**) and 10,13-bis(9,9-dimethylacridin-10(9H)-yl)dipyrido[3,2-a:2',3'-c]phenazine (**pDMAC-DPPZ**). Two 9,9-dimethyl-9,10-dihydroacridine (DMAC) donor units were attached at the *ortho* (11, 12) and *para* (10, 13) positions of the dipyrido[3,2-a:2',3'-c]phenazine (DPPZ) acceptor to obtain **oDMAC-DPPZ** and **pDMAC-DPPZ**, respectively. Interestingly, the photoluminescence quantum yield, external quantum efficiency, and emission wavelength of the emitters varied depending on the substitution pattern of DMAC on DPPZ. The two emitters exhibited distinct photophysical and organic light-emitting diode (OLED) performances due to structural differences related to steric strain and dihedral angles. It is demonstrated that the *ortho* (11, 12) donor substitution on DPPZ is more effective in the design of high-performance red TADF OLEDs than the *para* (10, 13) substitution in terms of singlet–triplet energy gap and up-conversion rate constant. The *ortho*-substituted TADF emitter demonstrated a high EQE of 13.4% with color coordinates of (0.59, 0.40), whereas the *para*-substituted isomer displayed an EQE of 4.0% and color coordinates of (0.64, 0.35).

Received 2nd January 2022,
Accepted 21st March 2022

DOI: 10.1039/d2tc00017b

rsc.li/materials-c

Introduction

Organic light-emitting diodes (OLEDs), proven to be superior to conventional liquid crystal displays, have been studied extensively for their solid-state lighting and display applications.^{1–6} Although state-of-the-art commercialized OLEDs are based on phosphorescent emitters, their demerits include the use of expensive noble metals, a low environmental sustainability, and short device lifetimes. Therefore, alternatives to phosphorescent OLEDs (Ph-OLEDs) are actively being sought. Organic-emitter-based thermally activated delayed fluorescent (TADF)-OLEDs are considered competent alternatives to Ph-OLEDs, as internal quantum efficiencies of up to 100% are achievable in both cases.^{7–13} Compared to precious-metal-based phosphorescent emitters, TADF emitters are inexpensive and allow for greater diversity in their design. Organic materials with a small singlet–triplet energy gap (ΔE_{ST}) are capable of converting non-radiative triplet excitons to radiative singlet excitons *via* a reverse intersystem crossing (RISC) process. A small ΔE_{ST} is achievable by minimizing the overlap between the

highest occupied molecular orbital (HOMO) and the lowest unoccupied molecular orbital (LUMO). Another requirement for the high-performance TADF emitters is a high photoluminescence quantum yield (PLQY), attainable by maintaining a maximum overlap between the HOMO and LUMO in the molecular design. Therefore, two contradictory requirements, a small ΔE_{ST} and high PLQY, need to be balanced in a single organic molecule to realize a high external quantum efficiency (EQE).

Recently reported high-performance blue and green TADF emitters have been constructed either by introducing new donor/acceptor moieties or *via* novel molecular design approaches.^{14–20} As red is a primary color, red TADF OLEDs are equally important as the blue and green TADF OLEDs. However, the red TADF emitters deliver significantly lower EQEs than blue and green TADF emitters, primarily because of the fundamental limitation of the energy gap theory.^{21,22} Because of the small band gap of the red TADF emitters, internal conversion, that is, non-radiative decay, dominates over radiative decay in this spectral region. To resolve this issue, various molecular design strategies have been developed and novel electron-accepting units have been introduced to simultaneously achieve high PLQY and small ΔE_{ST} values and deliver efficient long-wavelength TADF emitters.^{23–27} To avoid

School of Chemical Engineering, Sungkyunkwan University, 2066, Seobu-ro, Jangan-gu, Gyeonggi, Suwon 440-746, Korea. E-mail: leej17@skku.edu
† Electronic supplementary information (ESI) available. See DOI: [10.1039/d2tc00017b](https://doi.org/10.1039/d2tc00017b)

non-radiative loss mechanisms resulting from the vibrational and rotational motions of phenyl-spacer-based flexible structures, molecular designs wherein the donor unit is directly attached to the planar and rigid acceptor unit are preferred for the construction of the red TADF emitters.^{28–33} Among the available electron-withdrawing acceptor units, dipyrido[3,2-*a*:2,3-*c*]phenazine (DPPZ) has been investigated for the design of highly efficient red TADF emitters because of its rigid and fully conjugated planar heteroaromatic structure.^{34–37} Recently, it was demonstrated that the PLQYs of the red TADF emitters can vary significantly according to the donor substitution pattern on planar and rigid acceptors, such as phenanthro[4,5-*fgh*]quinoxaline-10,11-benzene^{38,39} and dibenzo[*a,c*]phenazine.⁴⁰ According to the energy gap law, the PLQY of TADF emitters decreases as their emission wavelength shifts toward the deep-red/near infrared region. Therefore, molecular designs that ensure high PLQYs in this region are crucial. To suppress non-radiative loss mechanisms and generate pure-color highly efficient TADF emitter-based OLEDs, the molecular designs wherein donor/acceptor rotation is restricted are preferred over those allowing for a free rotation.^{41–46} Recently, it was reported that the device performances of long wavelength TADF emitters can be largely varied depending upon the *ortho/para* donor substitution position,^{34,40,47} and the contribution of the locally excited triplet states in the emission process was studied to improve the RISC process of the *ortho* substituted TADF emitters over the *para* substituted derivatives.^{48,49}

In this study, DPPZ, as an acceptor, was disubstituted with 9,9-dimethyl-9,10-dihydroacridine (DMAC), as a donor, in two distinct patterns to generate two red TADF emitters, namely 11,12-bis(9,9-dimethylacridin-10(9H)-yl)dipyrido[3,2-*a*:3',2'-*c*]phenazine (***o*DMAC-DPPZ**) and 10,13-bis(9,9-dimethylacridin-10(9H)-yl)dipyrido[3,2-*a*:2',3'-*c*]phenazine (***p*DMAC-DPPZ**), which are configurational isomers of each other. The photophysical performances of the two isomeric TADF emitters were then evaluated to determine

the effects of the donor substitution pattern on the TADF properties. The EQEs and electroluminescence (EL) spectra of the two isomers differed significantly; the *ortho*-substituted TADF emitter, ***o*DMAC-DPPZ**, demonstrated a high EQE of 13.4% with color coordinates of (0.59, 0.40), whereas the *para*-substituted isomer, ***p*DMAC-DPPZ**, displayed an EQE of 4.0% and color coordinates of (0.64, 0.35). The effect of donor substitution pattern of the DPPZ acceptor derived TADF emitters was clearly revealed in this work.

Results and discussion

Molecular simulation and synthesis

To estimate the effects of the DMAC/DPPZ substitution pattern, time-dependent density functional theory (TD-DFT) calculations were performed for ***o*DMAC-DPPZ** and ***p*DMAC-DPPZ** in the ground state using the B3LYP/6-31G (d,p) basis set in the gas phase. The frontier molecular orbital diagrams of the two emitters with their HOMO–LUMO energy gaps and singlet–triplet energies are shown in Fig. 1. As expected, the HOMOs and LUMOs of both compounds were largely located over the DMAC donor and DPPZ acceptor segments, respectively. The HOMO–LUMO gap values were calculated to be 2.34 and 2.29 eV for ***o*DMAC-DPPZ** and ***p*DMAC-DPPZ**, respectively, indicating a red-shifted emission for the latter. Based on their small ΔE_{ST} values (0.0826 eV and 0.0094 eV for ***o*DMAC-DPPZ** and ***p*DMAC-DPPZ**, respectively), the involvement of triplet excitons in the emission process can be predicted. Because the DMAC donor was directly attached to the DPPZ acceptor, large dihedral angles of 77.1° and 85.7° were obtained for ***o*DMAC-DPPZ** and ***p*DMAC-DPPZ**, respectively (Fig. S1 in ESI†). The small dihedral angle in ***o*DMAC-DPPZ** suggests a more prominent HOMO–LUMO overlap in this emitter, and consequently, a higher PLQY in the red region.

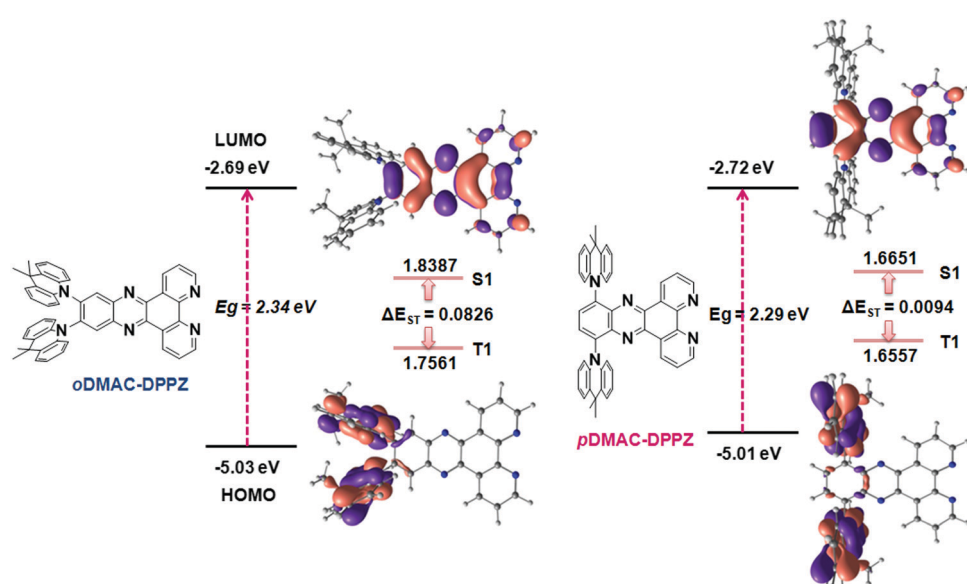
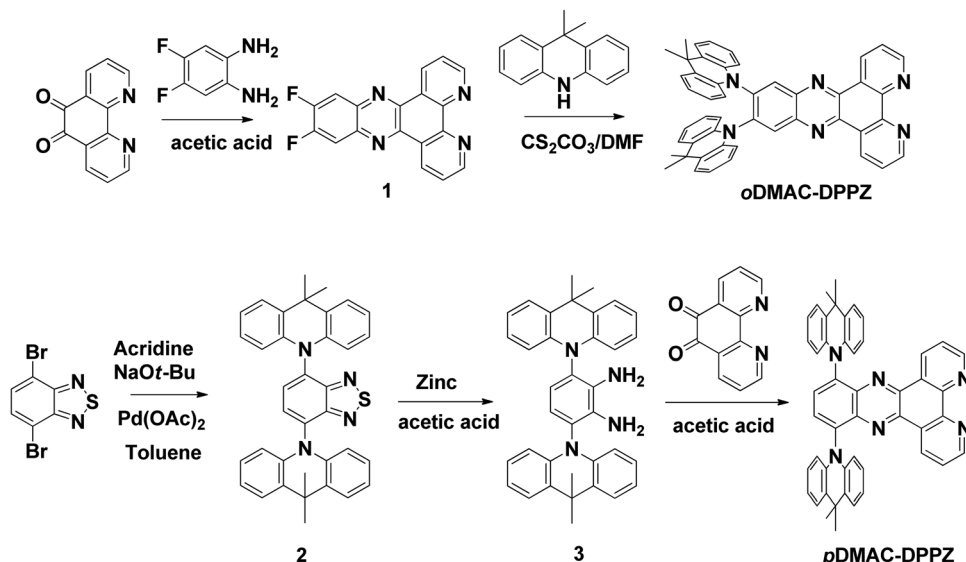


Fig. 1 Structures of ***o*DMAC-DPPZ** and ***p*DMAC-DPPZ** TADF emitters, and their ground state optimized geometries, HOMO–LUMO frontier molecular orbital diagrams, and HOMO–LUMO and singlet (S₁)–triplet (T₁) energies, calculated using DFT method.

Scheme 1 Synthetic route to ***o***DMAC-DPPZ and ***p***DMAC-DPPZ TADF emitters.

***o*DMAC-DPPZ** and ***p*DMAC-DPPZ** are synthesized according to the reaction sequence presented in Scheme 1. Intermediate 1 was readily obtained in good yield by cyclizing 1,10-phenanthroline-5,6-dione and 4,5-difluorobenzene-1,2-diamine. Intermediate 2 was synthesized according to a literature procedure,⁵⁰ and subsequently reduced to intermediate 3. Finally, intermediate 3 was cyclized with 1,10-phenanthroline-5,6-dione to obtain ***p*DMAC-DPPZ** in good yield.

Photophysical properties

The photophysical properties of the two TADF emitters were investigated to determine the effect of the DMAC substitution position on their absorption and emission features, singlet-triplet energies, and the TADF phenomenon. Ultraviolet-visible (UV-vis) and photoluminescence (PL) spectra were recorded in toluene at room temperature (Fig. 2a and b). The high-energy

peaks in their absorption spectra (330–400 nm) can be assigned to $n-\pi^*$ and $\pi-\pi^*$ transitions from the DMAC donor, as well as the DPPZ acceptor units, while the low-energy broad absorption peaks (420–600 nm) are attributed to the internal charge transfer (ICT) from the DMAC donor to the DPPZ acceptor unit. Notably, the intensity of the ICT absorption peak of ***o*DMAC-DPPZ** was higher than that of ***p*DMAC-DPPZ**, suggesting that the charge transfer (CT) properties of the two emitters were dependent on the substitution positions of the DMAC donor unit on the DPPZ acceptor. As predicted by DFT, the UV-vis absorption and PL spectra of ***p*DMAC-DPPZ** were slightly red-shifted compared to those of ***o*DMAC-DPPZ**. The singlet and triplet energies of both emitters were calculated from the onset of their fluorescence and phosphorescence, which were measured in toluene at 77 K (Fig. S2 in ESI†). The singlet-triplet energy gaps (ΔE_{ST}) calculated for ***o*DMAC-DPPZ** and ***p*DMAC-DPPZ** were 0.037 and 0.079 eV, respectively; these values were sufficiently small for an efficient RISC process to occur. The

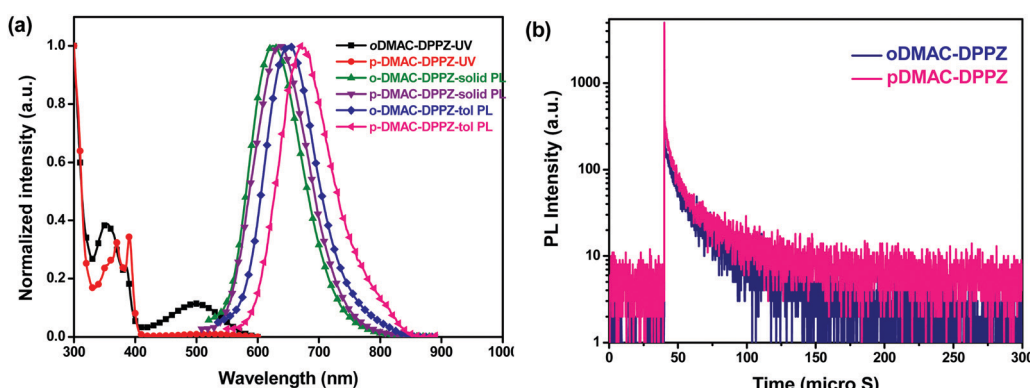


Fig. 2 (a) UV-vis absorption and PL spectra of ***o*DMAC-DPPZ** and ***p*DMAC-DPPZ** TADF emitters in toluene and those of 1% TADF-emitter-doped PS films at room temperature. (b) Transient PL decay curves of 1 wt% ***o*DMAC-DPPZ**- and ***p*DMAC-DPPZ**-doped thin PS films acquired at 300 K under a nitrogen atmosphere.

Table 1 Photophysical properties of *o*DMAC-DPPZ and *p*DMAC-DPPZ

Emitter	λ_{abs}^a [nm] sol	λ_{PL}^a [nm] sol	Φ_{PL}^b [%]	τ_p^c [ns]	τ_d^c [μs]	HOMO ^d [eV]	LUMO ^d [eV]	E_S/E_T^e [eV]	ΔE_{ST}^f [eV]
<i>o</i> DMAC-DPPZ	354, 499	652	63	27.02	1.76	-5.78	-3.59	2.26/2.23	0.037
<i>p</i> DMAC-DPPZ	390, 520	669	15	10.13	5.03	-5.73	-3.62	2.25/2.17	0.079

^a UV-Vis absorption and photoluminescence (PL) λ_{max} measured in toluene at 300 K. ^b Obtained by integrating sphere measurements. ^c PL lifetimes of prompt (τ_p) and delayed (τ_d) decay components measured in 1 wt% TADF-emitter-doped polystyrene films under a nitrogen atmosphere at 300 K. ^d Obtained from the oxidation and reduction onset potentials determined from the cyclic voltammograms. ^e Singlet (S1) and triplet (T1) energies. ^f $\Delta E_{\text{ST}} = E_S - E_T$.

structureless and broad fluorescence and phosphorescence spectra of both emitters indicate ICT-dominated singlet and triplet excited states. The photophysical properties of the two emitters are summarized in Table 1.

The TADF phenomenon was further investigated by measuring the photoluminescence quantum yield (Φ_{PL}) and transient PL decay of polystyrene (PS) films doped with the emitters (1 wt%) under a nitrogen atmosphere at room temperature. Table 1 summarizes the Φ_{PL} and PL lifetimes of the prompt (τ_p) and delayed (τ_d) decay components of the doped films. The Φ_{PL} of *p*DMAC-DPPZ (15%) was lower than that of *o*DMAC-DPPZ (63%), presumably because the singlet energy of the former was lower, as per the energy-gap law, as well as the degree of HOMO-LUMO overlap, compared to that of the latter. Fig. 2b shows the transient PL decay curves of the two emitters, which exhibited typical TADF decay values with nanosecond-order, τ_p , and microsecond-order, τ_d , under degassed conditions at room temperature. The short-lifetime, τ_p , values are related to a direct emission from the singlet state, while the long-lifetime, τ_d , values are associated with TADF, involving ISC and RISC processes. The τ_p and τ_d lifetimes of the *o*DMAC-DPPZ-doped PS film were estimated to be 27.0 ns and 1.8 μs, respectively, while those of the *p*DMAC-DPPZ-doped PS film were 10.1 ns and 5.0 μs, respectively (Table 1). The short delayed decay lifetime (1.7 μs) of the *o*DMAC-DPPZ emitter can be correlated

with its low ΔE_{ST} value (0.037 eV), suggesting that an efficient TADF process can be expected for this emitter.

To find out the contribution of locally excited triplet state (${}^3\text{LE}_A$) in the emission process, phosphorescence emission of DPPZ acceptor unit was measured in toluene solvent at low temperature (Fig. S10, ESI†). From the edge of the phosphorescence spectra, the triplet energy of the acceptor unit (${}^3\text{LE}_A$) was calculated to be 2.37 eV. Emission mechanism of *o*DMAC-DPPZ- and *p*DMAC-DPPZ TADF emitters was drawn in Fig. 3. Though the prompt fluorescence (PF) of both the emitter is similar, their delayed fluorescence (DF) mechanism is different and mainly affected by the locally excited triplet state of the acceptor unit (${}^3\text{LE}_A$) in the *o*DMAC-DPPZ TADF emitter. As compared to the *p*DMAC-DPPZ TADF emitter, the energy gap between charge transfer (${}^1\text{CT}$) and locally excited (${}^3\text{LE}_A$) triplet states of *o*DMAC-DPPZ TADF emitter was decreased to enhance the RISC process between singlet and triplet excited charge transfer states (${}^1\text{CT}$ and ${}^3\text{CT}$) through the contribution of ${}^3\text{LE}_A$. The small energy gap for vibrational coupling between ${}^1\text{CT}$ and ${}^3\text{LE}_A$ is responsible for the quick and efficient RISC of *o*DMAC-DPPZ.

The contribution of prompt (Φ_F) and delayed component (Φ_{TADF}) to the total Φ_{PL} was calculated and the respective rate constants of prompt and delayed component (k_p and k_d) were calculated using the values of Φ_F and Φ_{TADF} . Similarly, the rate

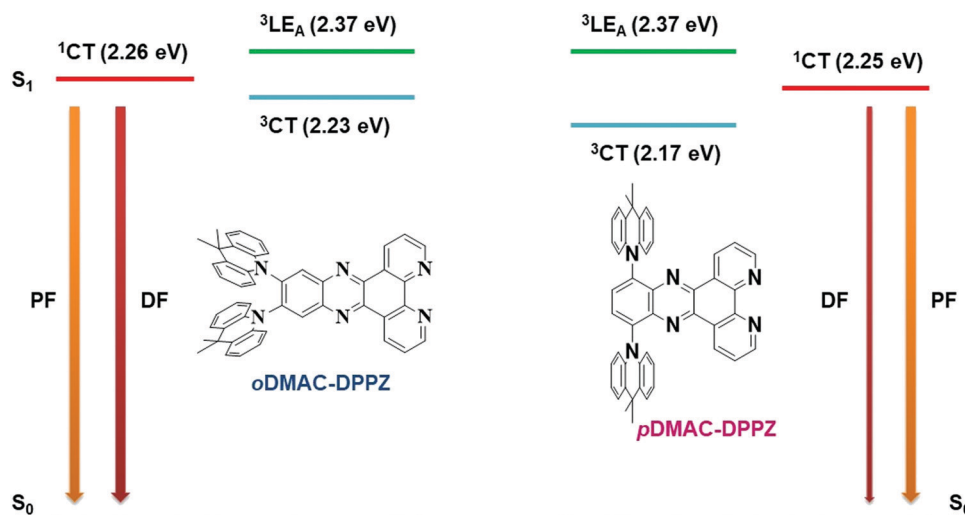


Fig. 3 Energy level diagram of *o*DMAC-DPPZ and *p*DMAC-DPPZ explaining the contribution of locally excited triplet state (${}^3\text{LE}_A$) of DPPZ acceptor in the RISC process of the *o*DMAC-DPPZ TADF emitter.

Table 2 Transient PL related photophysical parameters (Φ_F , Φ_{TADF} , k_p , k_d , k_{ISC} , k_{RISC} , k_r and k_{nr}) of *o*DMAC-DPPZ and *p*DMAC-DPPZ TADF emitters

Emitter	Φ_F [%]	Φ_{TADF} [%]	k_p [$\times 10^7$ s $^{-1}$]	k_d [$\times 10^5$ s $^{-1}$]	k_{ISC} [$\times 10^7$ s $^{-1}$]	k_{RISC} [$\times 10^6$ s $^{-1}$]	k_{RISC}/k_{ISC}	k_r [$\times 10^6$ s $^{-1}$]	k_{nr} [$\times 10^5$ s $^{-1}$]
<i>o</i> DMAC-DPPZ	0.09	0.54	3.70	5.68	3.39	4.01	0.1384	3.12	2.29
<i>p</i> DMAC-DPPZ	0.01	0.14	9.87	1.99	9.76	2.47	0.0253	1.11	1.71

constant values of intersystem crossing and reverse intersystem crossing (k_{ISC} and k_{RISC}) were calculated from the respective values of Φ_F/k_p and Φ_{TADF}/k_d , respectively. All the transient PL related parameters were calculated using the equations reported earlier²⁶ and are summarized in Table 2. In the two TADF emitters, comparatively higher k_d and k_{RISC} values (5.68×10^5 and 4.01×10^6 s $^{-1}$) were obtained for the *o*DMAC-DPPZ emitter because of its comparatively small ΔE_{ST} value (0.037 eV) and short delayed fluorescence lifetime (1.76 μ s) relative to that of the *p*DMAC-DPPZ emitter (0.079 eV and 5.03 μ s). The k_{RISC}/k_{ISC} ratio of *o*DMAC-DPPZ TADF emitter was higher (0.14) than that of the *p*DMAC-DPPZ TADF emitter (0.02), confirming effective triplet exciton utilization in this emitter. The k_{RISC} values (4.01 and 2.47×10^6 s $^{-1}$) of both emitters were much higher than their respective k_{nr} values (2.29 and 1.71 $\times 10^5$ s $^{-1}$), suggesting effective utilization of triplet excitons by both emitters in the red region. However, the EQE of *p*DMAC-DPPZ was decreased because of its low PLQY value (15%).

Thermal and electrochemical properties

The thermogravimetric analysis (TGA) of *o*DMAC-DPPZ and *p*DMAC-DPPZ was performed at a heating rate of 10 °C min $^{-1}$ under a nitrogen atmosphere, to evaluate their thermal stability at elevated temperatures. Fig. S3 (ESI †) presents the TGA curves of the two TADF emitters. The decomposition temperature of both emitters was very high (>400 °C) at 5% weight loss, confirming their excellent thermal stability, and thus, their suitability for vacuum-evaporation-based device fabrication. Cyclic voltammetry measurements were performed to investigate the effect of the DMAC substitution pattern on the HOMO-LUMO energy levels of the two compounds using a conventional three-electrode system. As expected, lower oxidation/reduction potential values were obtained for *p*DMAC-DPPZ (0.92/−1.18 V) compared to those of *o*DMAC-DPPZ (0.97/−1.22 V) (Fig. S4, ESI †). The HOMO and LUMO energy levels of the TADF emitters were calculated from the corresponding oxidation and reduction onset potential values. The HOMO/LUMO energy levels of *p*DMAC-DPPZ and *o*DMAC-DPPZ were calculated to be −5.73/−3.62 eV and −5.78/−3.59 eV, respectively. A relatively small HOMO-LUMO energy gap was obtained for the *p*DMAC-DPPZ emitter (2.11 eV) than the *o*DMAC-DPPZ emitter (2.19 eV). Therefore, a slightly more red-shifted emission wavelength can be predicted for *p*DMAC-DPPZ, compared to that of *o*DMAC-DPPZ.

Electroluminescence performance

Finally, *o*DMAC-DPPZ- and *p*DMAC-DPPZ-doped OLEDs were fabricated, and their performances were evaluated.

The OLED devices were fabricated using *o*DMAC-DPPZ or *p*DMAC-DPPZ as TADF emitters; poly(3,4-ethylenedioxythiophene):poly(styrenesulfonate) (PEDOT:PSS), 4,4'-cyclohexylidene-bis[N,N-bis(4-methylphenyl)aniline] (TAPC), and 1,3,5-tris(N-phenylbenzimidazol-2-yl)benzene (TPBi) as the hole-injection layer, hole-transporting layer, and electron-transporting layer, respectively; *N,N*-dicarbazolyl-3,5-benzene (mCP) and diphenyl-4-triphenylsilyl phenyl phosphine oxide (TSPO1) as the high triplet energy and hole- and electron-transport type exciton blocking layers, respectively; and 2-phenyl-4,6-bis(12-phenylindolo[2,3-*a*]carbazole-11-yl)-1,3,5-triazine (PBICT) as a bipolar host material to ensure high EQEs. The devices were structured as follows: indium tin oxide (ITO, 50 nm)/PEDOT: PSS (60 nm)/TAPC (20 nm)/mCP (10 nm)/PBICT-TADF emitter (25 nm: 1, 3, and 5 wt%)/TSPO1 (5 nm)/TPBi (40 nm)/LiF (1.5 nm)/Al (200 nm). Fig. 4 shows the energy level diagrams and chemical structures of the materials used in the devices. The Current density-voltage-luminance ($J-V-L$), EQE-luminance and EL spectra of the *o*DMAC-DPPZ and *p*DMAC-DPPZ-doped OLEDs are shown in Fig. 5 and Fig. S5 (ESI †), and the values of key device parameters are summarized in Table 3.

The EL spectra emitted by the OLED devices resembled those of TADF PL emission, confirming that the EL emission had originated exclusively from the emitter without any host material interference. *o*DMAC-DPPZ exhibited a red emission at 614 nm with the Commission Internationale de L'Eclairage (CIE) coordinates of (0.59, 0.40) and *p*DMAC-DPPZ exhibited a

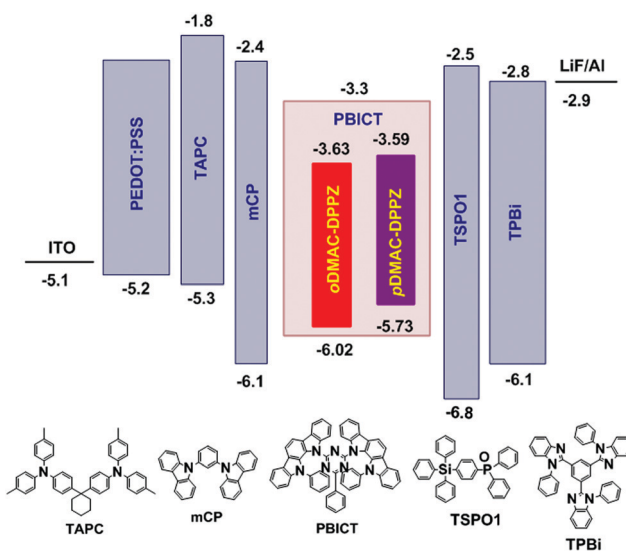


Fig. 4 Energy-level diagrams and chemical structures of the materials used in the OLEDs doped with *o*DMAC-DPPZ and *p*DMAC-DPPZ TADF emitters.

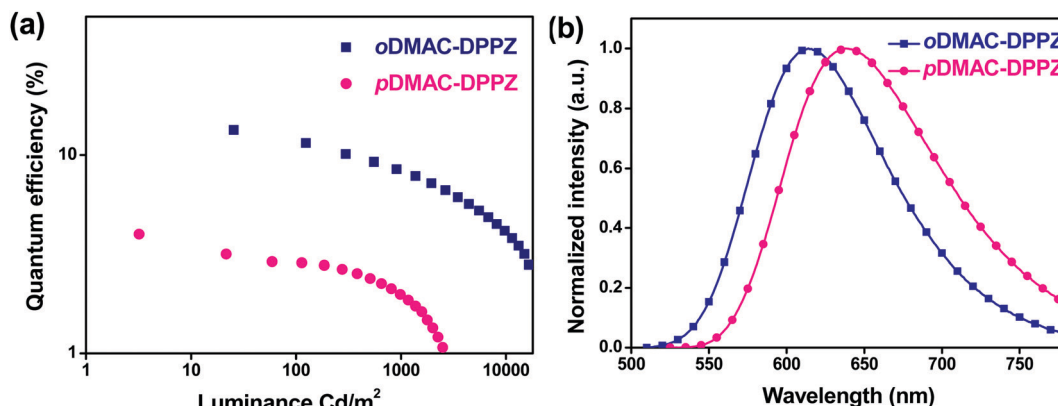


Fig. 5 (a) EQE–luminance characteristics, and (b) EL spectra of *o*DMAC–DPPZ- and *p*DMAC–DPPZ-doped OLEDs (1% doping concentration).

Table 3 Electroluminescence performances of the *o*DMAC–DPPZ- and *p*DMAC–DPPZ-emitter-based orange-red TADF-OLEDs at 1% doping concentration

Emitter	λ_{EL} [nm]	CE_{max} [cd A ⁻¹]	PE_{max} [lm W ⁻¹]	EQE_{max} [%]	CIE (x, y)
<i>o</i> DMAC–DPPZ	614	21.1	18.9	13.4	(0.59, 0.40)
<i>p</i> DMAC–DPPZ	638	4.2	3.8	4.0	(0.64, 0.35)

red-shifted emission at 638 nm with the CIE coordinates of (0.64, 0.35). Consistent with the high Φ_{PL} value of *o*DMAC–DPPZ (63%), the OLED doped with this emitter exhibited a high current efficiency of 21.1 cd A⁻¹, high power efficiency of 18.9 lm W⁻¹, and high EQE of 13.4%, while for the *p*DMAC–DPPZ-doped OLED, these values were 4.2 cd A⁻¹, 3.8 lm W⁻¹, and 4.0%, respectively. Both the devices exhibit maximum EQE values at a low doping concentration of 1 wt%, decreasing with increasing doping concentrations owing to the concentration quenching effect, as shown in Fig. S6 and S7 (ESI†). The EL spectra of both the devices were further red shifted with increasing doping concentrations of 1 to 5 wt% (Fig. S8 and S9, ESI†). From the above results, it can be concluded that the *ortho* donor substitution at positions 11 and 12 of the DPPZ acceptor resulted in a better OLED performance than that of the *para*-substituted TADF emitter.

Conclusion

Two configurational isomers of long-wavelength TADF emitters were synthesized to study the effect of the donor substitution pattern on their OLED performances. The *ortho*-substituted TADF emitter, *o*DMAC–DPPZ, exhibited a higher PLQY (63%) than the *para*-substituted isomer, *p*DMAC–DPPZ (15%) due to efficient RISC process assisted by small ΔE_{ST} . The red TADF-OLED doped with *o*DMAC–DPPZ exhibited a considerably higher EQE (13.4%) than the *p*DMAC–DPPZ-doped OLED (4.0%). Therefore, it was demonstrated that donor substitution at the *ortho* (11, 12) position of the DPPZ acceptor is preferred to the *para* (10, 13) substitution in the design of high-performance long-wavelength TADF emitters.

Experimental

Synthesis

Detailed synthetic procedures for the TADF emitters are given in the Supporting Information.

Device fabrication and measurements

The respective layers of the device were deposited *via* vacuum thermal evaporation under a high pressure of 3.0×10^{-7} Torr. Following the thermal evaporation of each material, the device was placed under a glass lid in a nitrogen-filled glove box to exclude moisture and oxygen. The electrical characterization of the devices was performed using a Keithley 2400 source meter, and optical characterization was conducted using a CS 2000 spectroradiometer.

Conflicts of interest

There are no conflicts to declare.

Acknowledgements

This work was supported by the Ministry of Trade, Industry, and Energy (20006464).

References

- 1 K. Goushi and C. Adachi, *Appl. Phys. Lett.*, 2012, **101**, 23306.
- 2 K. Goushi, K. Yoshida, K. Sato and C. Adachi, *Nat. Photonics*, 2012, **6**, 253.
- 3 M. Y. Wong and E. Zysman-Colman, *Adv. Mater.*, 2017, **29**, 1605444.
- 4 Z. Yang, Z. Mao, Z. Xie, Y. Zhang, S. Liu, J. Zhao, J. Xu, Z. Chi and M. P. Aldred, *Chem. Soc. Rev.*, 2017, **46**, 915–1016.
- 5 Y. Liu, C. Li, Z. Ren, S. Yan and M. R. Bryce, *Nat. Rev. Mater.*, 2018, **3**, 18020.
- 6 S. S. Kothavale and J. Y. Lee, *Adv. Opt. Mater.*, 2020, **8**, 2000922.
- 7 P. Jiang, J. Miao, X. Cao, H. Xia, K. Pan, T. Hua, X. Lv, Z. Huang, Y. Zou and C. Yang, *Adv. Mater.*, 2021, 2106954.

8 Y. Chen, D. Zhang, Y. Zhang, X. Zeng, T. Huang, Z. Liu, G. Li and L. Duan, *Adv. Mater.*, 2021, **33**, 2103293.

9 D. Karthik, Y. H. Jung, H. Lee, S. Hwang, B.-M. Seo, J.-Y. Kim, C. W. Han and J. H. Kwon, *Adv. Mater.*, 2021, **33**, 2007724.

10 C.-C. Peng, S.-Y. Yang, H.-C. Li, G.-H. Xie, L.-S. Cui, S.-N. Zou, C. Poriel, Z.-Q. Jiang and L.-S. Liao, *Adv. Mater.*, 2020, **32**, 2003885.

11 W. Li, Z. Li, C. Si, M. Y. Wong, K. Jinnai, A. K. Gupta, R. Kabe, C. Adachi, W. Huang, E. Zysman-Colman and I. D. W. Samuel, *Adv. Mater.*, 2020, **32**, 2003911.

12 S. Kothavale, K. H. Lee and J. Y. Lee, *Chem. – Eur. J.*, 2020, **26**, 845–852.

13 S. Kothavale, K. H. Lee and J. Y. Lee, *Chem. – Asian J.*, 2020, **15**, 122–128.

14 T.-A. Lin, T. Chatterjee, W.-L. Tsai, W.-K. Lee, M.-J. Wu, M. Jiao, K.-C. Pan, C.-L. Yi, C.-L. Chung, K.-T. Wong and C.-C. Wu, *Adv. Mater.*, 2016, **28**, 6976–6983.

15 D. R. Lee, B. S. Kim, C. W. Lee, Y. Im, K. S. Yook, S.-H. Hwang and J. Y. Lee, *ACS Appl. Mater. Interfaces*, 2015, **7**, 9625–9629.

16 C. Li, C. Duan, C. Han and H. Xu, *Adv. Mater.*, 2018, **30**, 1804228.

17 D. H. Ahn, S. W. Kim, H. Lee, I. J. Ko, D. Karthik, J. Y. Lee and J. H. Kwon, *Nat. Photonics*, 2019, **13**, 540–546.

18 D. R. Lee, M. Kim, S. K. Jeon, S.-H. Hwang, C. W. Lee and J. Y. Lee, *Adv. Mater.*, 2015, **27**, 5861–5867.

19 T.-L. Wu, M.-J. Huang, C.-C. Lin, P.-Y. Huang, T.-Y. Chou, R.-W. Chen-Cheng, H.-W. Lin, R.-S. Liu and C.-H. Cheng, *Nat. Photonics*, 2018, **12**, 235–240.

20 Y. Kondo, K. Yoshiura, S. Kitera, H. Nishi, S. Oda, H. Gotoh, Y. Sasada, M. Yanai and T. Hatakeyama, *Nat. Photonics*, 2019, **13**, 678–682.

21 J. V. Caspar, E. M. Kober, B. P. Sullivan and T. J. Meyer, *J. Am. Chem. Soc.*, 1982, **104**, 630–632.

22 S. D. Cummings and R. Eisenberg, *J. Am. Chem. Soc.*, 1996, **118**, 1949–1960.

23 Q. Zhang, H. Kuwabara, W. J. Potscavage, S. Huang, Y. Hatae, T. Shibata and C. Adachi, *J. Am. Chem. Soc.*, 2014, **136**, 18070–18081.

24 J. Li, T. Nakagawa, J. MacDonald, Q. Zhang, H. Nomura, H. Miyazaki and C. Adachi, *Adv. Mater.*, 2013, **25**, 3319–3323.

25 I. S. Park, S. Y. Lee, C. Adachi and T. Yasuda, *Adv. Funct. Mater.*, 2016, **26**, 1813–1821.

26 S. Kothavale, K. H. Lee and J. Y. Lee, *ACS Appl. Mater. Interfaces*, 2019, **11**, 17583–17591.

27 S. Kothavale, W. J. Chung and J. Y. Lee, *J. Mater. Chem. C*, 2021, **9**, 528–536.

28 S. Kothavale, W. J. Chung and J. Y. Lee, *ACS Appl. Mater. Interfaces*, 2020, **12**, 18730–18738.

29 S. Wang, Y. Miao, X. Yan, K. Ye and Y. Wang, *J. Mater. Chem. C*, 2018, **6**, 6698–6704.

30 C. Zhou, C. Cao, D. Yang, X. Cao, H. Liu, D. Ma, C.-S. Lee and C. Yang, *Mater. Chem. Front.*, 2021, **5**, 3209–3215.

31 U. Balijapalli, Y.-T. Lee, B. S. B. Karunathilaka, G. Tumen-Ulzii, M. Auffray, Y. Tsuchiya, H. Nakanotani and C. Adachi, *Angew. Chem., Int. Ed.*, 2021, **60**, 19364–19373.

32 P. Data, P. Pander, M. Okazaki, Y. Takeda, S. Minakata and A. P. Monkman, *Angew. Chem., Int. Ed.*, 2016, **55**, 5739–5744.

33 S. Kothavale, J. Lim and J. Yeob Lee, *Chem. Eng. J.*, 2022, **431**, 134216.

34 B. Zhao, H. Wang, C. Han, P. Ma, Z. Li, P. Chang and H. Xu, *Angew. Chem., Int. Ed.*, 2020, **59**, 19042–19047.

35 H. Wang, B. Zhao, P. Ma, Z. Li, X. Wang, C. Zhao, X. Fan, L. Tao, C. Duan, J. Zhang, C. Han, G. Chen and H. Xu, *J. Mater. Chem. C*, 2019, **7**, 7525–7530.

36 J.-X. Chen, K. Wang, C.-J. Zheng, M. Zhang, Y.-Z. Shi, S.-L. Tao, H. Lin, W. Liu, W.-W. Tao, X.-M. Ou and X.-H. Zhang, *Adv. Sci.*, 2018, **5**, 1800436.

37 J.-X. Chen, W.-W. Tao, W.-C. Chen, Y.-F. Xiao, K. Wang, C. Cao, J. Yu, S. Li, F.-X. Geng, C. Adachi, C.-S. Lee and X.-H. Zhang, *Angew. Chem., Int. Ed.*, 2019, **58**, 14660–14665.

38 A. Shang, T. Lu, H. Liu, C. Du, F. Liu, D. Jiang, J. Min, H. Zhang and P. Lu, *J. Mater. Chem. C*, 2021, **9**, 7392–7399.

39 T. Yang, Z. Cheng, Z. Li, J. Liang, Y. Xu, C. Li and Y. Wang, *Adv. Funct. Mater.*, 2020, **30**, 2002681.

40 C. Zhou, W.-C. Chen, H. Liu, X. Cao, N. Li, Y. Zhang, C.-S. Lee and C. Yang, *J. Mater. Chem. C*, 2020, **8**, 9639–9645.

41 Y. J. Cho, S. K. Jeon, S.-S. Lee, E. Yu and J. Y. Lee, *Chem. Mater.*, 2016, **28**, 5400–5405.

42 G. Meng, X. Chen, X. Wang, N. Wang, T. Peng and S. Wang, *Adv. Opt. Mater.*, 2019, **7**, 1900130.

43 D.-Y. Chen, W. Liu, C.-J. Zheng, K. Wang, F. Li, S. Tao, X.-M. Ou and X.-H. Zhang, *ACS Appl. Mater. Interfaces*, 2016, **8**, 16791–16798.

44 Z.-P. Chen, D.-Q. Wang, M. Zhang, K. Wang, Y.-Z. Shi, J.-X. Chen, W.-W. Tao, C.-J. Zheng, S.-L. Tao and X.-H. Zhang, *Adv. Opt. Mater.*, 2018, **6**, 1800935.

45 J. Jayakumar, T.-L. Wu, M.-J. Huang, P.-Y. Huang, T.-Y. Chou, H.-W. Lin and C.-H. Cheng, *ACS Appl. Mater. Interfaces*, 2019, **11**, 21042–21048.

46 T.-L. Wu, S.-H. Lo, Y.-C. Chang, M.-J. Huang and C.-H. Cheng, *ACS Appl. Mater. Interfaces*, 2019, **11**, 10768–10776.

47 W. Xie, M. Li, X. Peng, W. Qiu, Y. Gan, Z. Chen, Y. He, W. Li, K. Liu, L. Wang, Q. Gu and S.-J. Su, *Chem. Eng. J.*, 2021, **425**, 131510.

48 J.-X. Chen, Y.-F. Xiao, K. Wang, D. Sun, X.-C. Fan, X. Zhang, M. Zhang, Y.-Z. Shi, J. Yu, F.-X. Geng, C.-S. Lee and X.-H. Zhang, *Angew. Chem., Int. Ed.*, 2021, **60**, 2478–2484.

49 H. Wang, L. Zhou, Y.-Z. Shi, X.-C. Fan, J.-X. Chen, K. Wang, J. Yu and X.-H. Zhang, *Chem. Eng. J.*, 2022, **433**, 134423.

50 F. Ni, Z. Wu, Z. Zhu, T. Chen, K. Wu, C. Zhong, K. An, D. Wei, D. Ma and C. Yang, *J. Mater. Chem. C*, 2017, **5**, 1363–1368.